



Experimental Investigation and Modelling of Damage Evolution/Propagation in Carbon/Epoxy Laminated Composites

C. L. Chow

Department of Mechanical Engineering, University of Hong Kong,
Hong Kong

X. J. Xian & J. Lam

Institute of Mechanics, Chinese Academy of Sciences,
Beijing, People's Republic of China

(Received 13 April 1989; revised version received 2 October 1989;
accepted 14 November 1989)

ABSTRACT

Experimental and theoretical analyses to characterize the damage propagation of carbon/epoxy composite laminates with varying layups, notch/crack geometries and crack lengths are presented. Different damage processes were examined, using Moiré interferometry, acoustic emission and infrared thermography tests. A damage propagation model, based on the equivalent crack propagation concept, is proposed to predict the various stages of damage evolution/propagation and the fracture strength. The predictions agree well with the experimental results of earlier investigations.

INTRODUCTION

Advanced composite materials of high performance are generally brittle. During manufacturing processes and in service conditions, either internal and/or surface damage is developed; the damage area may be large but with negligible plastic deformation. The ultimate failure process for such

materials often results from the formation and propagation of multiple damage, such as matrix cracking, interface debonding, delamination, fibre breakage, etc. Because the various types of damage in composites are more complicated than those of conventional materials, it is necessary to conduct experimental investigations to characterize each damage mode properly. Based on observations and measurements, a model may then be deduced, and numerical data predicted from the model can be compared with experimental results^{1,2} to test the validity of the model. Although various techniques have been used to identify separately the various modes of damage in composites,³⁻⁶ only a few workers have ventured to use advanced techniques systematically to monitor and cross-check the results during the entire damage process. The latter is considered important to obtain unbiased conclusions, which may vary depending upon the particular experimental technique at an investigator's disposal.

With respect to damage analysis, the conventional models used for prediction of tensile strength of notched composite laminates are based primarily on macroscopic fracture stress criteria. These include the inherent flaw model (IFM) proposed by Waddoups *et al.*,⁷ and the point stress criterion (PSC) and average stress criterion (ASC) proposed by Whitney and Nuismer,^{8,9} all of which adopt macroscopic fracture strength as a fracture parameter. The mean stress criterion takes into account the effect of anisotropy and damage zone on the fracture behavior of composites, and yields better agreement with experiments than do other criteria. The micro-mechanical theory advocated by Mar and Lim¹⁰ proposed a semi-empirical method to predict rapid fracture formulation which included the effect of bi-material interfacial behavior at the crack tip emanating from a circular hole. Although the model addressed certain aspects of material damage, it did not pay sufficient attention to the overall damage process. The damage zone model (DZM) proposed by Hillerborg *et al.*¹¹ attempted to characterize the damage evolution process, and yielded good agreement with experiment.

This paper is intended to present a series of damage measurements using different experimental techniques which are used to check the validity of a proposed damage propagation model for advanced composite laminates. Carbon/epoxy specimens of six stacking sequences $[0]_8$, $[0_3/90_2]_{2s}$, $[0/90]_{4s}$, $[90/0/\pm 45]_{2s}$, $[\pm 45]_{4s}$ and $[90]_8$, were fabricated without notch or with centre hole (CH), centre notch (CN) or single edge notch (SEN). The experimental techniques include Moiré interferometry, acoustic emission, IR thermography and scanning electron microscopy, which were used separately to observe the damage behaviors, so that the conclusions observed by one technique may be verified by others. Furthermore, a damage propagation model (DPM), based on the concept of equivalent crack propagation and damage process, is proposed to characterize different

stages of damage evolution/propagation and to predict tensile fracture strength. The damage propagation stages predicted using the proposed model are in general agreement with observations.

ANALYSIS

Development/initiation damage model

To characterize non-linear material behavior at the crack tip, Barenblatt¹² and Dugdale¹³ introduced a cohesive zone where the stresses assume a finite magnitude of, say, yield stress at the crack tip (Fig. 1). If the fibres in a composite are assumed to provide the cohesive force which links the crack surfaces, composite fracture may be brought within the scope of the crack

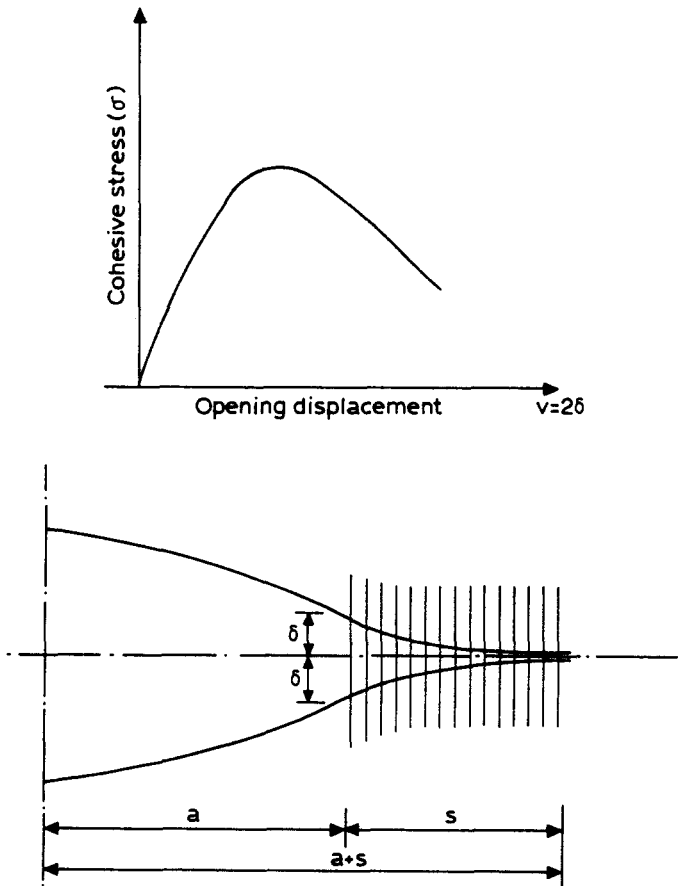


Fig. 1. Dugdale-Barenblatt model.

opening displacement (COD) concept of Dugdale and Barenblatt by postulating that the threshold condition of crack initiation is

$$V_c = 2\delta_c \quad (1)$$

where V_c is the critical total COD and δ_c is the critical COD (Fig. 1). The concept of critical COD has been shown to be consistent with the Griffith-Irwin energy equilibrium condition.¹³ For the determination of the critical release rate G_c , the crack surface relative opening and its associated non-linear zone length at the crack tip may then be used as an intrinsic material parameter to describe the critical state, i.e.

$$G_c = \int_0^{V_c} \sigma(V) dV \quad (2)$$

Damage/crack propagation model of composite laminates

In addition to the crack initiation model described above, the concept of COD may also be extended to characterize damage/crack propagation in composite laminates. This is achieved by using the concept of an equivalent crack to simulate the damage zone on the hole edge or at the crack tip (Fig. 2). Because of the effects of anisotropy, fibre orientation and multi-

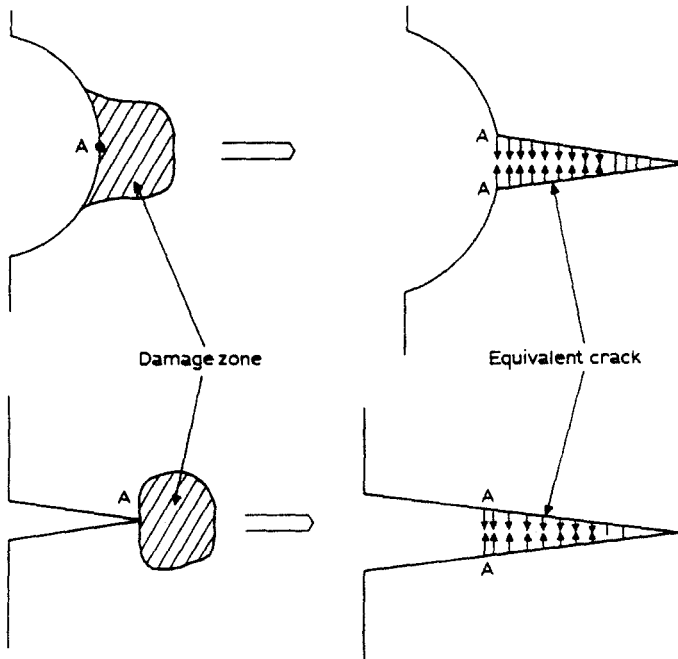


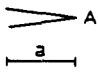
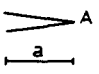
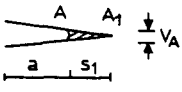
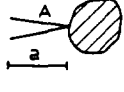
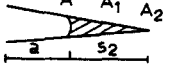
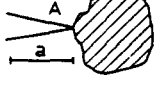
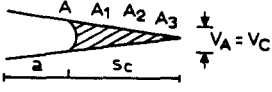

Fig. 2. Damage propagation model.

laminates structure on damage propagation, the model proposed has the following additional requirements:

- (1) There should be an equivalent critical damage energy release rate.
- (2) The process of damage propagation at the crack tip in laminates is assumed to be equivalent to crack propagation through the non-linear/cohesive zone in metals.
- (3) At the threshold of damage propagation, the COD δ at the notch tip reaches its critical value V_c .

The strain-energy release rate described in eqn (2) includes the energy dissipation of all forms of damage during damage evolution/propagation in laminates. The critical value of strain-energy release rate G_c is thus assumed to be an intrinsic material property, representing energy dissipation during the entire damage process up to failure. Although damage takes different forms in different composite laminates, damage evolution progressively develops to a certain critical state when failure finally occurs. The notch tip opening displacement $V = V_c$ is postulated to represent the critical state of actual damage propagation. Table 1 shows the progressive patterns of the damage propagation model (DPM) in the characterization of damage evolution/propagation. The model postulates that for brittle materials, such as graphite composites, there is no COD at point A of the crack length a shown in Table 1 when the applied load reaches P_0 or the stress σ at the crack

TABLE 1
Simulation of Damage Propagation

External load	Equivalent crack propagation			Damage propagation	
	σ	v	s	Pattern	
$P = P_0$	$\sigma_A = \sigma_0$	$V_A = 0$	$s = 0$		
$P_1 > P_0$	$\sigma_A \neq 0$ $\sigma_{A_1} = \sigma_0$	$V_A \neq 0$ $V_{A_1} = 0$	$s = s_1$		
$P = P_2$	$\sigma_A \neq 0$ $\sigma_{A_1} \neq 0$ $\sigma_{A_2} = \sigma_0$	$V_A \neq 0$ $V_{A_1} \neq 0$ $V_{A_2} = 0$	$s = s_2$		
$P = P_3$	$\sigma_A = 0$ $\sigma_{A_1} \neq 0$ $\sigma_{A_2} \neq 0$ $\sigma_{A_3} = \sigma_0$	$V_A = V_c$ $V_{A_1} \neq 0$ $V_{A_2} \neq 0$ $V_{A_3} = 0$	$s = s_c$		

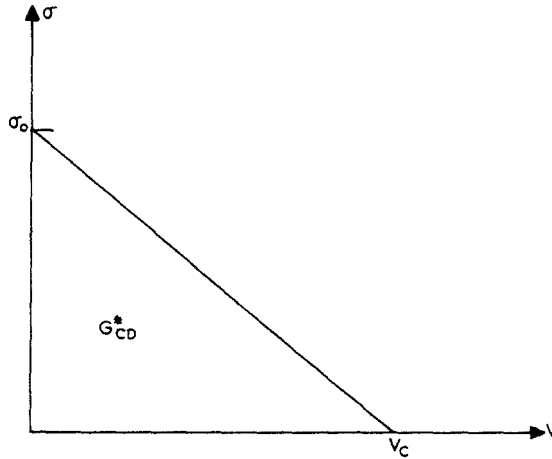


Fig. 3. σ - V curve of brittle material.

tip σ_A is raised to σ_0 . The stress σ_0 is taken as the tensile strength of the graphite composite system. However, further application of load at $P_1 > P_0$ induces damage development within the region S_1 , yielding the conditions that are postulated as $\sigma_A \neq 0$, $V_A \neq 0$, $\sigma_{A1} = \sigma_0$ and $V_{A1} = 0$ within the damage zone S_1 . Additional load application to P_2 causes enlargement of the damage zone to S_2 , where the stress and displacement conditions are assumed to be $\sigma_A \neq 0$, $V_A \neq 0$, $\sigma_{A1} \neq 0$, $\sigma_{A2} = \sigma_0$ and $V_{A2} = 0$. At the threshold condition of crack initiation of $V_A = V_c$ and $V_{A3} = 0$, when the applied load reaches $P = P_3$, the damage zone size becomes $S = S_c$, where the stress and displacement conditions are assumed to be $\sigma_{A1} \neq 0$, $V_{A1} \neq 0$, $\sigma_{A2} \neq 0$, $V_{A2} \neq 0$, $\sigma_{A3} = \sigma_0$, and $V_{A3} = 0$.

For brittle material, a linear relationship between crack opening V and stress σ may be assumed (Fig. 3), and has been found to yield good agreement with experiment in composite laminates.¹⁴ The crack opening displacement V and applied stress σ may accordingly be expressed as

$$\sigma = \sigma_0(1 - V/V_c) \quad (3)$$

As

$$G = J = \int_0^{V_c} \sigma(V) dV \quad (4a)$$

$$G_c = \sigma_0 V_c / 2 \quad (4b)$$

Accordingly, the equivalent critical energy release rate is defined as

$$G_{CD}^* = \sigma_0 V_c / 2 \quad (4c)$$

SPECIMENS AND EXPERIMENTAL METHODS

The specimens used in this study were made from T300 and S220 carbon fibres with 648 epoxy matrix. The fibre volume fraction was *c.* 65%. The stacking sequences of $[0]_8$, $[0_3/90_2]_{2s}$, $[0/90]_{4s}$, $[90/0/\pm 45]_{2s}$, $[\pm 45]_{4s}$ and $[90]_8$ were fabricated without notch, or with centre hole (CH), centre notch (CN) or single edge notch (SEN). Four aspect ratios of diameter (or centre notch) to specimen width (or $2R/w$ or $2a/w$), i.e. 0.15, 0.25, 0.3 and 0.4, were chosen for CH and CN specimens. The notches were machined by line electrode cutting, which produced a tip radius of 0.16 mm. Three aspect ratios, 0.15, 0.12 and 0.3, were adopted for single notch specimens. Details of the specimens are given in Table 2 and shown in Fig. 4. σ_0 described in the table denotes the tensile strength of unnotched specimens, and σ_r and σ_n denote the tensile strength of notched specimens based respectively on gross and net cross-sectional area.

The tensile tests were conducted using an MTS universal testing machine, with a strain rate of 1 mm/min. Moiré interferometry tests were carried out using a loading fixture which was fixed on a vibration-isolation table.

The magnitude of deformation of composite materials is very small but has high strain gradient under loading. As Moiré interferometry can produce high-sensitivity whole-field contour maps of in-plane displacement, the method was chosen to provide U and V displacement fields for damage analysis in carbon/epoxy laminates.¹⁵ The method entails the use of a high-frequency crossed-grid (600 lines/mm) diffraction grating which was replicated on the specimen surface by means of a special mold. This yielded a thin (0.025 mm) reflective-phase grating which firmly adhered to the

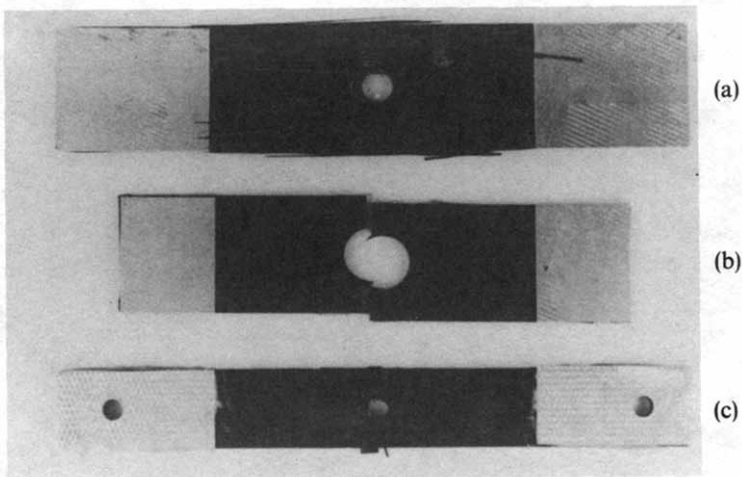


Fig. 4. Failure mode of composite with centre hole.

TABLE 2
Specimens and Experimental Results in Tension

Materials	Specification	Unnotched				C/H				C/V				S/E _N			
		σ_0 (MPa)	$2r^a$	$2r/w$	σ_c^b	σ_n^b	σ_v/σ_0	$2a$	$2a/w$	σ_t	σ_n	σ_v/σ_0	a	a/w	σ_t	σ_n	σ_v/σ_0
T300/648	[0] ₀ , AI-S	1847										3	0.2	1403	1767	0.76	
	AI-S'																
	[0/90] ₄ , AIV-S	997	15.2	0.4	20.9	34.7	0.33					4.5	0.3	1373	1804	0.75	
	[90] ₁₈ , BIII-H	63.7	15.2	0.4	16.7	278	0.36					3	0.2	776	973	0.78	
S220/648	[90/0/±45] ₂ , BIV-H	467															
	BIV-C							13.2	0.3	194	298	0.4					
	[0], CI-H	968	3	0.15	849	1132	0.88										
	, CI-H'		5	0.125	902	1061	193										
[±45] ₄ , CII-C	CI-C							6	0.3	585	834	0.60					
	CII-H	133	3	0.15	101	119	0.76										
	CII-H'		5	0.25	81.4	108	0.61										
	DII-H	102	3	0.15	68.8	96.7	0.68										
[0 _v /90 ₂] ₂ , DIV-H	DII-H'		5	0.25	58.8	68.8	0.58										
	DIV-H	896	10	0.25	596	852	0.67										
[0/90] ₄ , CIV-C		671	3	0.15	337	481	0.50										

^a r is hole radius.

^b σ_t and σ_n are tensile strength of notched specimen based respectively on gross and net cross-sectional area.

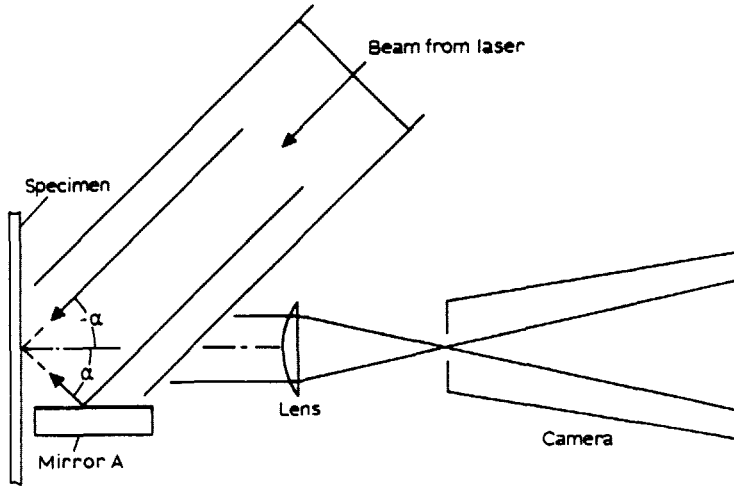


Fig. 5. Optical arrangement for Moiré interferometry.

specimen and deformed with it. The initial frequency of specimen grating chosen was $f/2$ before load application, which produced a reference grating frequency of 1200 lines/mm. Figure 5 illustrates the experimental set-up, together with pertinent rays for the system with a real reference grating. The frequency of each virtual reference grating is $f = (2 \sin \alpha) / \lambda$, where λ is the wavelength of the light and α is the angle between the incident beam and the normal to the reference grating. Each reference grating interacts with similarly oriented lines of the specimen grating to form interference patterns, which are recorded by a camera. The patterns which were taken in an interval of loading, ΔP , are contour maps of displacements governed by the relationships

$$U = \frac{1}{f} N_x \quad \text{and} \quad V = \frac{1}{f} N_y \tag{5}$$

where U and V are the fringe orders. Strains are finally evaluated from the displacement fields by the relations (small strain)

$$\begin{aligned} \epsilon_x &= \frac{\partial u}{\partial x} = \frac{1}{f} \left(\frac{\partial N_x}{\partial x} \right) \\ \epsilon_y &= \frac{\partial v}{\partial y} = \frac{1}{f} \left(\frac{\partial N_y}{\partial y} \right) \\ \gamma_{xy} &= \frac{\partial u}{\partial y} + \frac{\partial v}{\partial x} = \frac{1}{f} \left(\frac{\partial N_x}{\partial y} + \frac{\partial N_y}{\partial x} \right) \end{aligned} \tag{6}$$

Figures 6–9 depict the damage-induced deformation fields of carbon/epoxy laminates with different notches using Moiré interferometry.

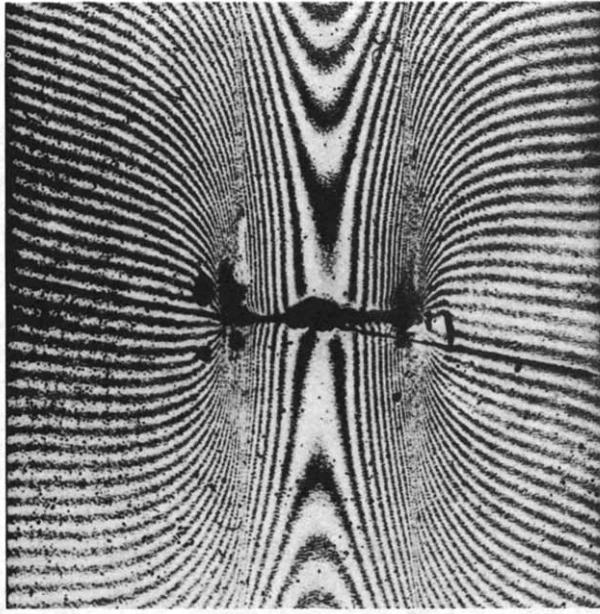
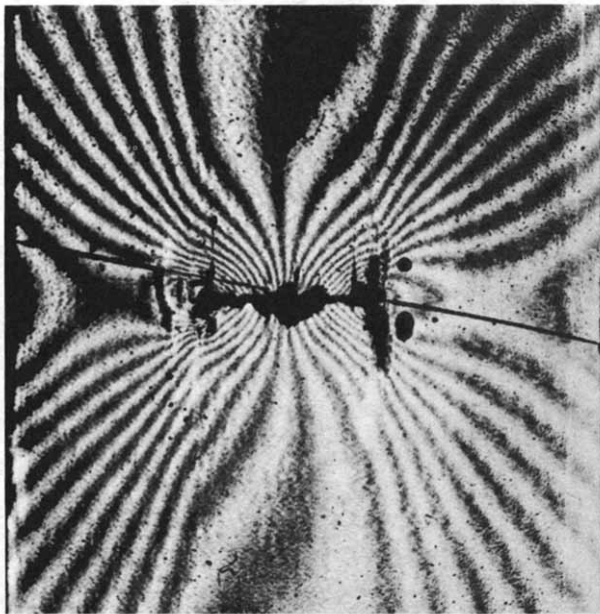
 U  V

Fig. 6. U and V displacement fields for the 0° -ply carbon/epoxy specimen with centre notch under initial loading.

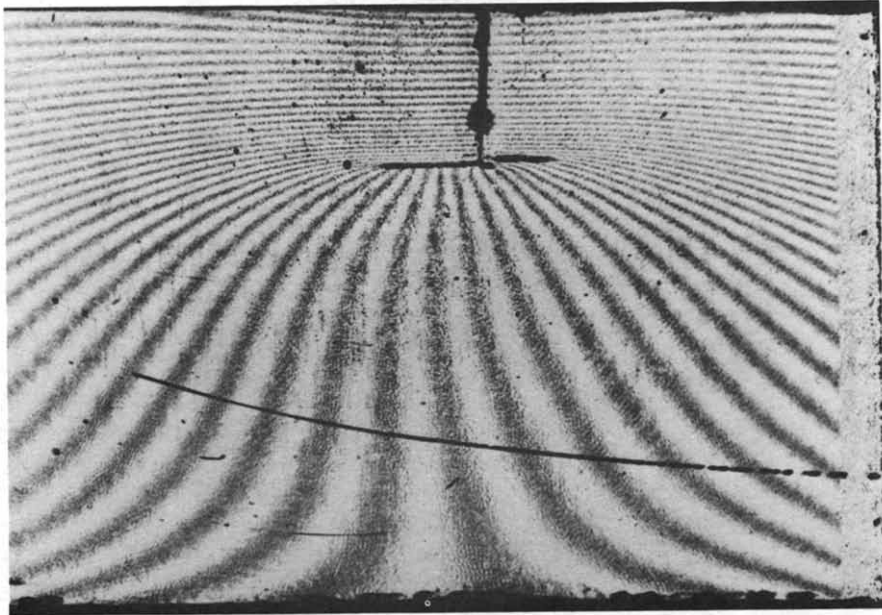


Fig. 7. U and V displacement fields for 0°-ply S1:N carbon/epoxy specimen with longitudinal crack at notch tip.

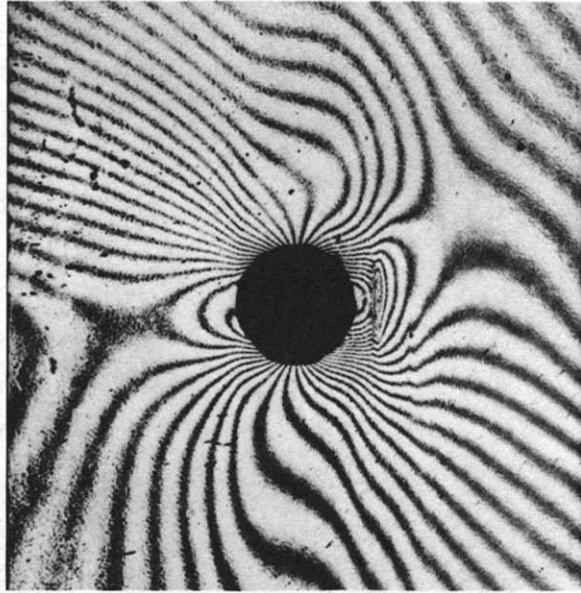
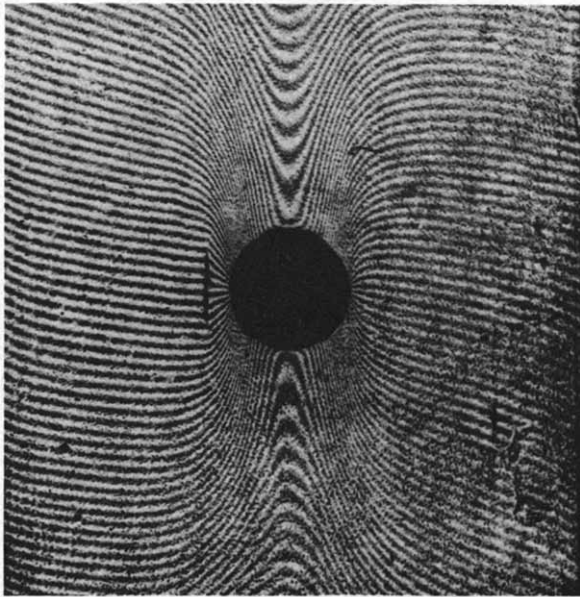
 U  V

Fig. 8. U and V displacement fields for the 0° -ply carbon/epoxy specimen containing a centre hole.

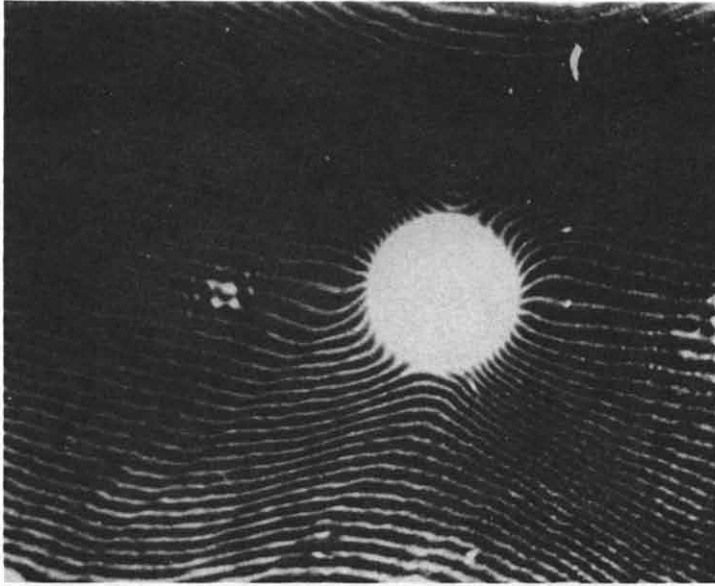


Fig. 9. *contd.* (b) U—elastic damage.

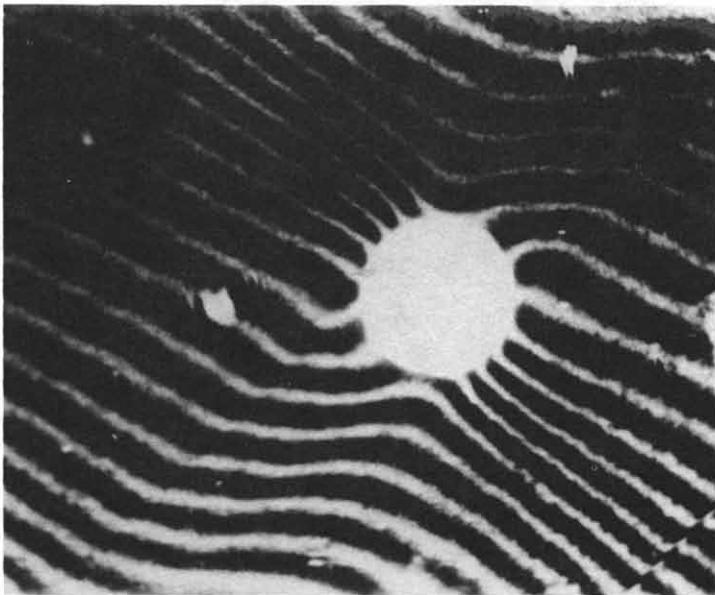


Fig. 9. Damage propagation of $\pm 45^\circ$ -ply specimen containing a centre hole, showing Moiré interferometry fringes. (a) U—Initial non-damage stage.

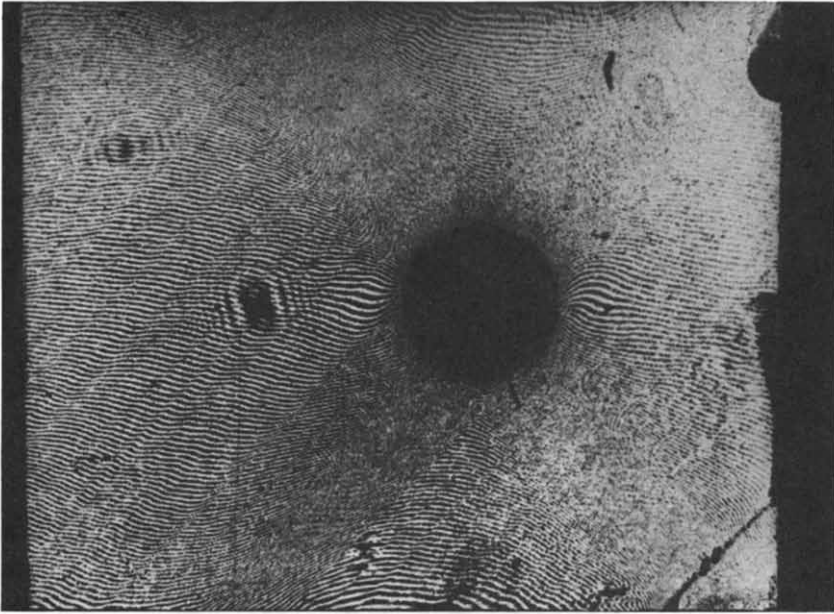


Fig. 9. *cont'd.* (d) Unsteady damage propagation.

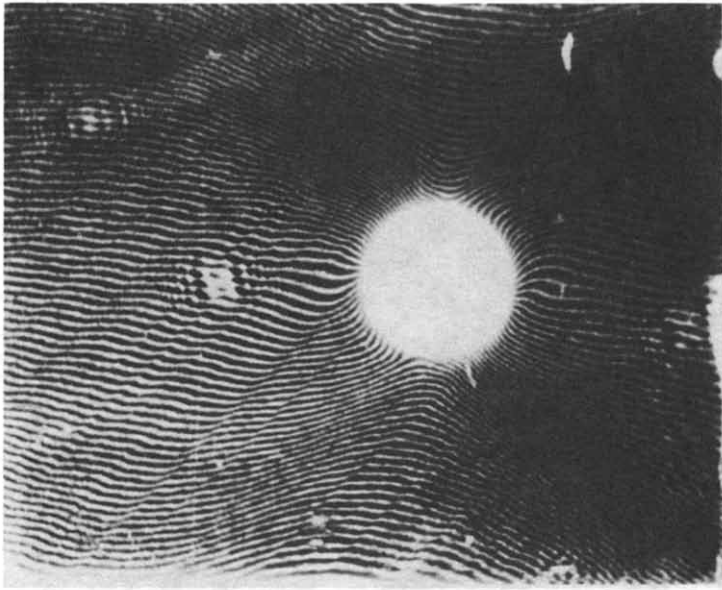


Fig. 9. *cont'd.* (c) *U*—inelastic damage.

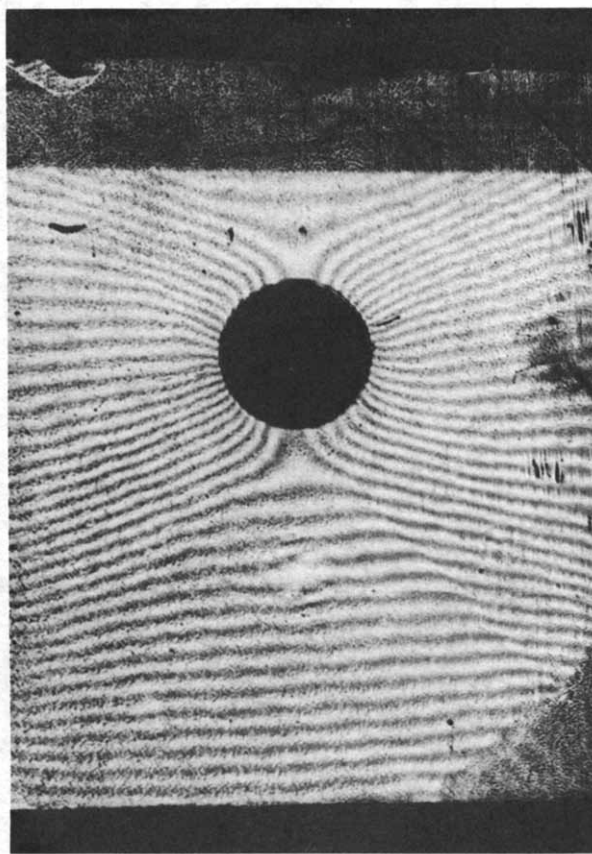


Fig. 9.—contd. (e) V field.

The damage evolution/propagation in the specimens was also detected using the acoustic emission technique (an SFS-4 AE system) during each test. Acoustic emission (AE) displays a transient elastic wave generated by the rapid release of energy within a material. Probes were mounted on each specimen to collect signals which were then amplified and recorded as a pattern, known as the AE count increase dN , or cumulative counts N . N is the function of deformation variable x . As the released rate of the composite's damage energy G_{CD}^* represents the damage propagation state of materials, thus

$$N = N(G_D^*) \quad N_c = N(G_{CD}^*)$$

G_{CD}^* is the critical energy release rate of damage and is related to the critical cumulative data N_c . The weighted ringdown signals are chosen as the characteristic parameter in this study. Figures 10–13 show the curves of

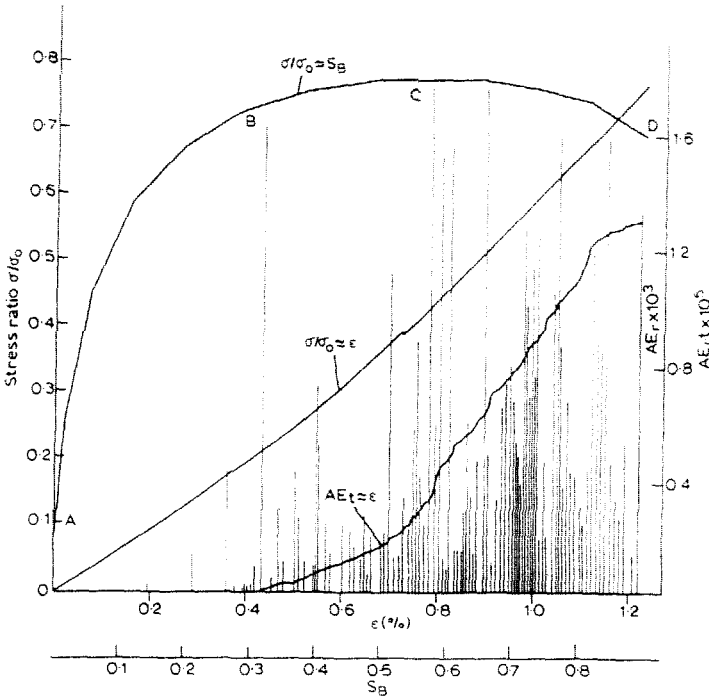


Fig. 10. Damage propagation pattern. ($\sigma/\sigma_0 \approx \epsilon$, $AE \approx \epsilon$, $\sigma/\sigma_0 \approx S_B$) of $[0]_n$ CH (CI-H3) specimen.

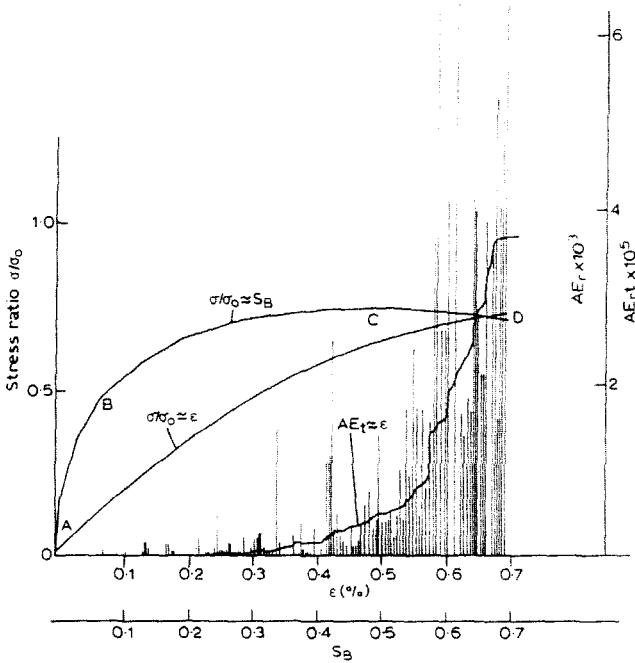


Fig. 11. Damage propagation pattern of $[\pm 45]_n$ CH (CII-H3) specimen.

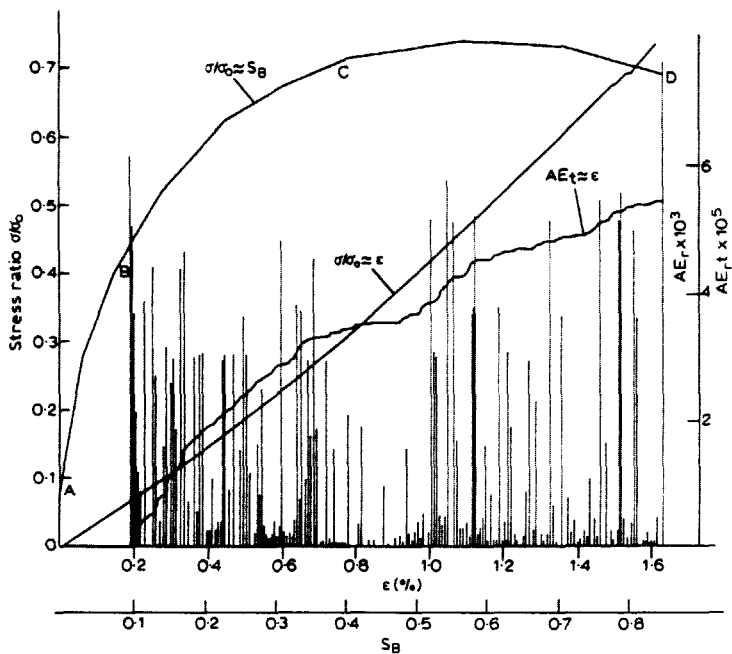


Fig. 12. Damage propagation pattern of $[0]_n$ SEN(Al-S) specimen.

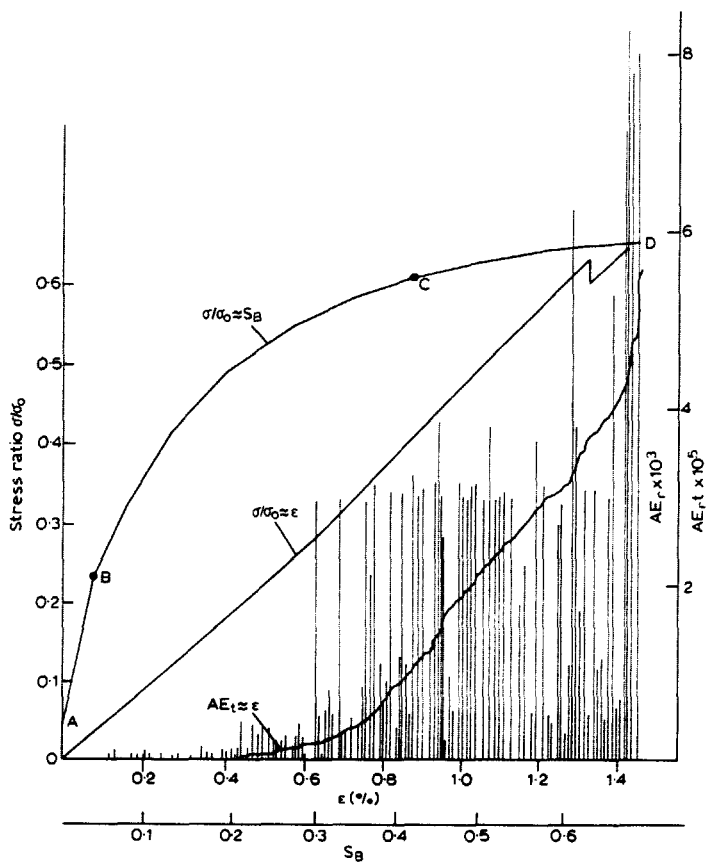


Fig. 13. Damage propagation pattern of $[90/0/\pm 45]_2$ SEN(AIV-S) specimen.

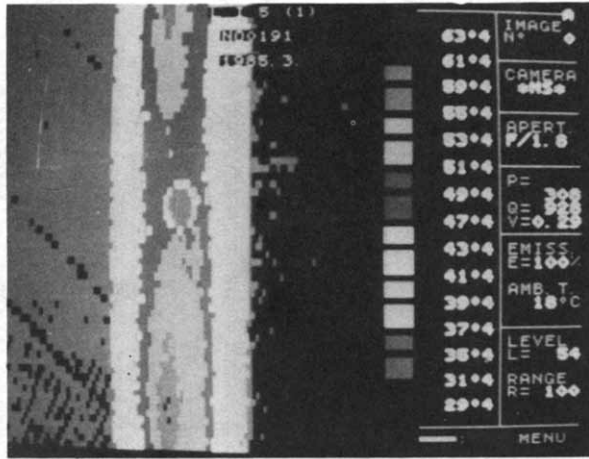


Fig. 14. Temperature field of 0-ply specimen with centre hole.

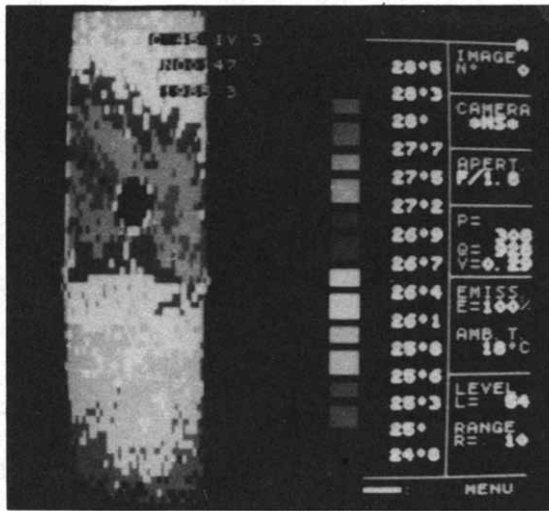
stress and strain ($\sigma/\sigma_0 \approx \epsilon$), the AE test results ($AE \approx \epsilon$) and the predicted damage evaluation propagation ($\sigma/\sigma_0 \approx S_B$). S_B is defined as the aspect ratio of the distance S of the cohesive damage zone to half of the specimen width $W/2$ or $S_B = S/W/2$.

An AGA 708 IR thermographic system was used to monitor the temperature variation (ΔT) and distribution in the specimens during the damage process. The degree of damage was evaluated according to the variation of ΔT , and the damage zone was examined using the lines of constant temperature (Figs 14 and 15). In addition, strain gage measurements were recorded to compare with the observations made with the above experimental techniques. Especially for hole/notch specimens, more than 10 gages were mounted around the hole/notch to detect the change in damage. Finally, the damage characteristics of the microstructure of various stacking sequences of laminates were examined by an S570 scanning electron microscope.

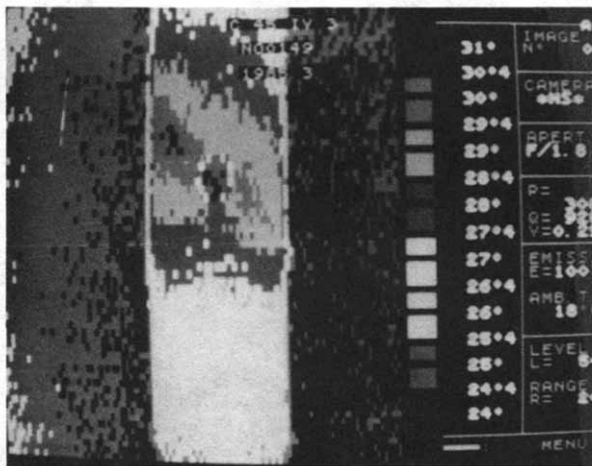
RESULTS

Experimental results and analysis

For each composite system, 3–5 specimens were manufactured and then tested. The measured mean stress values of various composite systems are summarized in Table 2. The stress of the notched specimens shown in Figs 10–13 is expressed in non-dimensional form as the ratio of the stress of gross cross-sectional area σ and σ_0 (σ/σ_0).



(a)



(b)

Fig. 15. Temperature field of $\pm 45^\circ$ -ply specimen with centre hole.

Table 3 shows the results of predicted strength σ_c (eqn (7)) for various laminates and the comparisons between experimental values and those calculated using the IFM, PSC and MSC models.⁷⁻⁹ It can be observed from the table that the critical strain energy release rates G_{CD}^* obtained from identical constituents and layups but with different notch types are about the same. G_{CD}^* was evaluated based on eqn (4c) from the measured value of V_c , defined as the critical crack opening displacement, and the tensile strength of

TABLE 3
Comparison of Experimental and Predicted Values

Material	Specification	G_{CB}^a (kJ/m ²)	IFM		PSC		MSC		DPM	
			σ_c^{IFM} (MPa)	δ^I (%)	σ_c^{PSC} (MPa)	δ^P (%)	σ_c^{MSC} (MPa)	δ^M (%)	σ_c^{DPM} (MPa)	δ^D (%)
T300/648	[0] ₈ AI-S	2000	1175	-16.3	1243	11.4	1055	-24.8	1287	-8.3
	AI-S'	2000	933	-26.8	989	22.3	808	-33.9	1122	-11.9
	[0/90] ₄ AIV-S	1500	543	-15.7	571	11.3	500	-22.5	614	-4.7
	[90] ₈ BIII-II	0.5	17.2	-17.2	17.4	16.3	12.5	-40.1	20.9	0.58
	[90/0/+45] ₃ BIV-H BIV-C	35 35	213 226	26.7 16.7	222 247	32.1 27.8	166 183	-0.9 -5.8	170 196	1.2 0.95
S220/648	[90] ₈ C1-H'	350	990	10.3	1049	16.9	878	-2.2	926	2.7
	C1-II	350	841	-0.9	882	3.8	775	-8.7	784	-7.7
	C1-C	350	738	26.17	782	33.7	623	6.4	596	1.9
	[±45] ₄ CII-II	9	117	15.5	123	21.9	108	7.0	103	1.7
	CII-H'	9	99.3	21.9	105	29.3	84.1	3.37	79.9	-1.8
	DII-II	8.5	94	36.6	98	42.4	88.5	28.6	81.7	18.8
	DII-H'	8.5	83.5	42	88.6	52	73.8	25.4	67.2	14.3
	[0 ₃ /90 ₃] ₆ DIV-C	900	684	14.7	726	21.7	580	-1.2	604	1.18
	[0/90] ₄ CIV-C	65	368	9.3	382	13.3	283	-15.9	331	-1.77

a. δ , σ_c , σ_1 , 100° , σ_1 - experimental fracture strength represented in Table 2.

the composite, σ_0 . The observed value is not unexpected as G_{CD}^* is a measure of energy dissipation more closely related to material characteristics and layups rather than to specimen geometry. G_{CD}^* was used to evaluate the characteristic distance c of the IFM, PSC and MSC models, which in turn allowed the determination of the tensile strength σ_c for the different models. The maximum deviation is 18.8% using the damage propagation model, whereas the deviations for the IFM and PSC models are larger (Table 3).

As the equivalent Young's modulus E_0 may be evaluated as

$$E_0 = \left[\frac{1}{2E_L E_T} (\sqrt{E_T/E_L} + \left(\frac{1}{G_{LT}} - \frac{2\nu_{LT}}{EL} \right) \frac{E_T}{2}) \right]^{-1/2}$$

then

$$\sigma_c = \left[\frac{G_{CD}^* E_0}{F^2(a/w)[\pi(a+c)]} \right]^{1/2} \quad (7)$$

where E_L is Young's modulus in the longitudinal direction, E_T is Young's modulus in the transverse direction, ν_{LT} is Poisson's ratio, G_{LT} is the shear modulus, F is a geometrical function of a/w , and $c = c_0$ is the characteristic length for the IFM model, $c = c_1$ for the PSC model and $c = c_2$ for the MSC model and other similar expressions.

Damage propagation

The predicted curves of different damage propagation may be divided into four stages in terms of the varying relationship between stress level (σ/σ_0) and the damage zone propagation rate S_B , as shown in Figs 10–13. S_B denotes the aspect ratio of the distance S of the cohesive damage zone (Fig. 1) to the specimen's half-width $W/2$, i.e. $S_B = SW/2$. Figures 10 and 11 depict the relationships of the tensile stress vs strain, AE vs strain and σ/σ_0 vs S_B for two typical specimens with a centre hole, of unidirectional ply $[0]_8$ CI-H3 and multi-directional ply $[\pm 45]_{4s}$ CII-H3.

During the first stage (I) or OA (see Figs 10–13), when the load was increased to a certain value, the laminates appeared to be in a non-damaged elastic state with no detectable AE signal. Figures 9(a) and (b) show the Moiré interferometric images of the corresponding stage of no damage. During the second stage (II) or AB, initial damage in the form of matrix cracking occurred, with an AE signal of low-energy release. The curve $\sigma/\sigma_0 \approx \varepsilon$ is shown to be linear, but the stress level rose rapidly during this stage. In the third state (III) or BC, the delamination damage developed rapidly at the hole edge along the fiber direction. The AE signal was thus enhanced and had a large value (Fig. 10). This stronger signal indicated the longitudinal cracking of the $[0]_8$ ply specimen or some delamination of the

$[\pm 45]_{4s}$ ply specimen, as shown in Figs 6, 7 and 9(c). Both the predicted and measured stress-strain curves of $[\pm 45]_{4s}$ are non-linear in this stage. Their damage region S_B is larger than for other composite systems, but the stress gradient is less than those of stage II. In the fourth and final stage (IV) or CD, fibers broke gradually and shear failure occurred progressively from one layer to another from the edge of the hole. Damage propagated unsteadily and the AE signal became stronger and more frequent. The AE cumulation increased rapidly and represented the release of total energy. No significant change in the stress level σ/σ_0 was observed, causing a decrease in the progressive specimen failure.

Damage propagation characteristics of various laminates

[90]_8 laminate

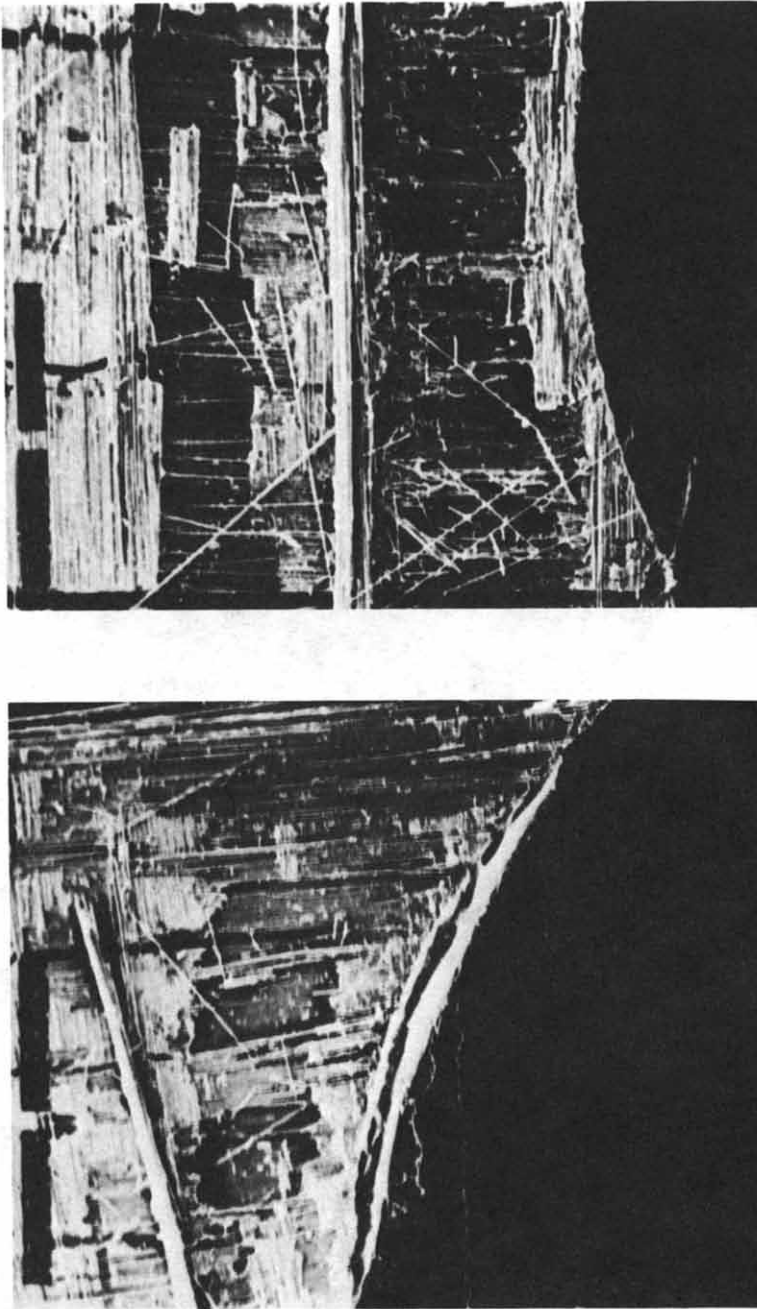
The damage propagation was governed by a process of equivalent crack propagation, which was very short, followed by sudden failure. Figure 4(c) shows the failure mode of a 90° -ply CH specimen.

[0]_8 laminate

Damage propagates from a high strain concentration at the notch-tip to a large area. Longitudinal cracks appear at the notch-tip and propagate towards the edge of the specimen. Figure 14 shows this dominant damage type for a 0° -ply specimen, by IR thermography. The load applied was mainly taken by the fibres, and fracture occurred because of the reduced cross-sectional area caused by fiber breakage. Figures 4(a), 6 and 7 show the interferometric fringes and failure modes of 0° -ply specimens with CH, CN and SEN specimens, respectively. Figure 12 shows the change of direction in damage during stages II and III, which agrees with the COD curve obtained by Czarnek and Post.¹⁵

$[\pm 45]_{4s}$ laminate

Figures 9(a)–9(e) represent the Moiré interferometric images of damage propagation in $\pm 45^\circ$ -ply CH specimens (CII-H1) under tensile loading. Initially, the distribution of strain fields $\partial u/\partial x$ and $\partial v/\partial y$ shown in Figs 9(a) and (e) were uniform, and there was no observed damage; $\pm 45^\circ$ damage bands were subsequently formed (Figs 9(b) and 9(c)). When the load increased to a critical level, the damage zone became intensified and enlarged to the extent that Moiré fringes were disrupted by the damage band (Fig. 9(d)). Finally, specimens failed by shear along the 45° direction. Figures 15(a) and (b) show the IR thermographic images of the specimen, which in some ways resemble the Moiré interferometric images. During the damage propagation shown in Fig. 15, a temperature rise ΔT was observed at the



(a) (b)
Fig. 16. Fracture surface of [90/0/±45] specimen (scanning electron micrograph).

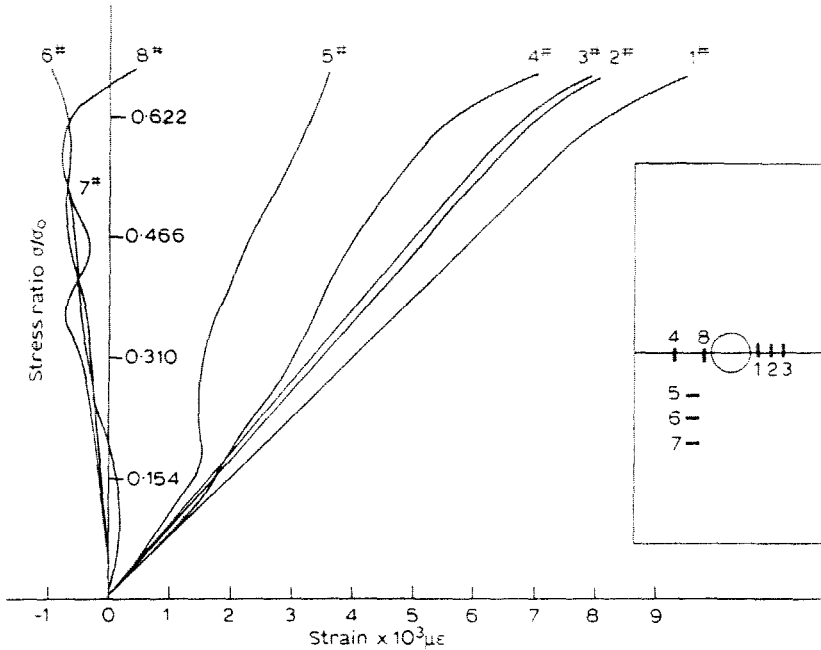


Fig. 17. Strain gage measurement of $[90/0 \pm 45]$ CH(DIV-H) specimen.

hole. At the 45° damage band, ΔT of 2 C was recorded, but in the undamaged zone, negligible ΔT values (0–0.4 C) were noted. The stress level at the ΔT peak appeared close to the change of direction in damage during stages II and III predicted by the DPM method.

$[90/0 \pm 45]_2$, laminate

In theory, the damage characteristics of this laminate system should contain all the elements of damage in individual 0° , 90° and $\pm 45^\circ$ ply laminates. Figures 16(a) and (b) show the fracture surfaces of a $[90/0/\pm 45]_{ns}$ specimen. Its damage stages II and III were observed to be longer. The recorded stress–stress curve shown in Fig. 13 reveals a sudden drop of load at about $0.6 \sigma/\sigma_0$, which indicates a sudden change in material behavior. This agrees with similar behavior observed from a separate testing of the same specimen using the strain gage technique shown in Fig. 17, which depicts the sudden change of direction of the measured stress at about $0.6 \sigma/\sigma_0$.

DISCUSSION AND CONCLUSIONS

Several advanced techniques, including Moiré interferometry, acoustic emission and IR thermography, which provide real-time measurement, are

separately used to monitor the entire damage evolution/propagation process, including the critical damage stage, of laminated composites. When AE and heat (induced by temperature rise) accumulation increased suddenly, the Moiré interferometry fringes changed suddenly from a uniform pattern to one with a sharp gradient in the damage zone, which indicated a rapid damage development known as critical damage.

From the computer results produced from the proposed damage propagation model (DPM) and from experimental observations for specimens loaded to fracture, the damage propagation processes can be subdivided into four stages:

Stage I, non-damage stage.

Stage II, initial damage linear propagation.

Stage III, damage non-linear propagation.

Stage IV, damage unsteady propagation.

Stage II together with stage III is known as the steady propagation stage. The transition from the steady to the unsteady stage shows damage characteristics which result from the increasing extent of damage (quantity) and the intensity of damage (quality). This transition point is identified as similar to the critical damage mentioned earlier. The stress level at the transition point may be considered as the threshold point of composite laminate fracture.

The predictions of fracture strength based on the proposed damage propagation model agree well with the experimental results, for several experimental techniques.

ACKNOWLEDGEMENT

This work was supported in part by the National Natural Science Foundation Committee of China under contract 1860360.

The authors express their appreciation for assistance in the tests by Dr A. Asundi and Mr M. T. Cheung.

REFERENCES

1. Chow, C. L. & Xian, X. J., Fracture behaviour of carbon/epoxy composites with damage consideration. *J. Reinf. Plastics*, **8**(1) (1989) 55-78.
2. Xian, X. J., Static and fatigue failure behaviour of carbon fiber reinforced epoxy composite materials with edge notch. *Sci. Sinica, Ser. A*, **27**(5) (1984) 547-58.
3. Post, D., Moiré interferometry for damage analysis of composites. *Exp. Techniques*, **7**(7) (1983) 17-20.

4. Nahas, M. N., Analysis of composite failure mechanism using acoustic emission and ultrasonic scanning techniques. *Composites*, **16**(2) (1985) 148–52.
5. Norio, S., Toshio, K. & Osami, K., Detection of damage in composite materials by thermo-acoustic emission measurement. *J. Composite Mater.*, **22** (1988) 458.
6. Rarkash, R., Non-destructive testing of composites. *Composites*, **15**(3) (1984) 200–6.
7. Waddoups, M. E., Eiseman, J. R. & Kaminski, B. E., Macroscopic fracture mechanics of advanced composite materials. *J. Composite Mater.*, **5** (1971) 446–54.
8. Whitney, J. M. & Nuismer, R. J., Stress fracture criteria for laminated composites containing stress concentrations. *J. Composite Mater.*, **8** (1974) 253–65.
9. Nuismer, R. J. & Whitney, J. M., Uniaxial failure of composite laminates containing stress concentrations. ASTM STP 593, 1975, pp. 117–42.
10. Mar, J. W. & Lim, K. Y., Tensile fracture of laminates with holes. *J. Composite Materials*, **11** (1977) 405–21.
11. Hillerborg, A., Moclcer, M. & Petersson, P. E., Analysis of crack formation and crack growth in concrete by means of fracture mechanics and finite elements. *Cement Concrete Res.*, **6** (1976) 773–82.
12. Barenblatt, G. I., Mathematical theory of equilibrium crack in a brittle body. *Adv. Appl. Mech.*, **7** (1962) 55–60.
13. Dugdale, D. S., Yielding of steels containing slits. *J. Mech. Phys. Solids*, **8** (1960) 100–4.
14. Aronsson, C. G. & Backlund, J., Damage mechanics analysis of matrix effects in notched laminates. *ASTM Symp. Composite Materials: Fracture and Fatigue*. ASTM, 1984, pp. 287–306.
15. Czarnek, R. & Post, D., Moiré interferometry with 45-deg grating. *Exp. Mech.*, **24**(1) (1984) 68–74.